RSC Advances

PAPER

View Article Online
View Journal | View Issue

Cite this: *RSC Adv.*, 2022, **12**, 14342

Rational design of large flat nitrogen-doped graphene oxide quantum dots with green-luminescence suitable for biomedical applications

Michael Nazarkovsky,[a] Albina Mikhraliieva,[a] Carlos A. Achete,[b] Luiz Anastacio Alves,[c] Joyce Araujo,[b] Bráulio S. Archanjo,[b] José Júnior França de Barros,[d] Liana Monteiro da Fonseca Cardoso,[c] José Nelson S. S. Couceiro,[e] Fernanda Davi Marques,[b] Bruno S. Oliveira,[b] Rafael Nascimento Dias de Souza,[b] Ayla Josma Teixeira,[c] Thiago L. Vasconcelos[b] and Vladimir Zaitsev *[af]

Rational synthesis and simple methodology for the purification of large (35–45 nm in lateral size) and flat (1.0–1.5 nm of height) nitrogen-doped graphene oxide quantum dots (GOQDs) are presented. The methodology allows robust metal-free and acid-free preparation of N-GOQDs with a yield of about 100% and includes hydrothermal treatment of graphene oxide with hydrogen peroxide and ammonia. It was demonstrated that macroscopic impurities can be separated from N-GOQD suspension by their coagulation with 0.9% NaCl solution. Redispersible in water and saline solutions, particles of N-GOQDs were characterized using tip-enhanced Raman spectroscopy (TERS), photoluminescent, XPS, and UV-VIS spectroscopies. The size and morphology of N-GOQDs were studied by dynamic light scattering, AFM, SEM, and TEM. The procedure proposed allows nitrogen-doped GOQDs to be obtained, having 60–51% of carbon, 34–45% of oxygen, and up to 7.2% of nitrogen. The N-GOQD particles obtained in two hours of synthesis contain only pyrrolic defects of the graphene core. The fraction of pyridine moieties grows with the time of synthesis, while the fraction of quaternary nitrogen declines. Application of TERS allows demonstration that the N-GOQDs consist of a graphene core with an average crystallite size of 9 nm and an average distance between nearest defects smaller than 3 nm. The cytotoxicity tests reveal high viability of the monkey epithelial kidney cells Vero in the presence of N-GOQDs in a concentration below 60 mg L^{-1}. The N-GOQDs demonstrate green luminescence with an emission maximum at 505 nm and sedimentation stability in the cell culture medium.

Received 8th March 2022
Accepted 8th April 2022

DOI: 10.1039/d2ra01516a

rsc.li/rsc-advances

1 Introduction

Carbon dots (CDs) is a general term that is currently used for a new class of carbonaceous fluorescent nanoscale objects[1–3] that was discovered in 2004 by the electrophoretic purification of oxidized single-wall carbon nanotubes.[4] CDs demonstrate photoluminescence (PL) not seen for earlier known fullerenes and nanodiamonds, can be obtained from various carbon-containing precursors in gram-scale,[5] and can produce stable suspensions in water. Unlike other photoluminescent nano-objects such as porous silicon,[6] metal halide perovskite nanocrystals,[7] and semiconductor quantum dots, CDs are metal-free nano-objects and thus they are much more environmentally friendly and biocompatible. Finally, the production and application of CDs are very sustainable. They can be obtained from various organic objects,[8] and degrade in a natural environment. Due to their low-toxic nature and biocompatibility CDs have great potential in biotechnology and nanomedicine,[1,9,10] cell imaging and biolabeling,[11–14] for drug release,[15] theranostics,[9,16] and photodynamic therapy.[17]

CDs can be synthesized using a wide variety of top-down and bottom-up approaches. The top-down one is based on the shredding of large carbon objects such as graphite, graphene oxide,[18] and nanodiamonds[19] by using arc discharge,[4] laser ablation,[20] chemical or electrochemical oxidation.[21] Bottom-up approach has been proposed more recently as an alternative

[a]*Department of Chemistry, Pontifical Catholic University of Rio de Janeiro, Marques de Sao Vicente, 225, 22451-900, Rio de Janeiro, Brazil*
[b]*Instituto Nacional de Metrologia, Qualidade e Tecnologia, Inmetro, Av. Nossa Senhora das Graças, 50, Xerém, Duque de Caxias, 25250-020, Brazil*
[c]*Laboratory of Cellular Communication, Oswaldo Cruz Institute, Oswaldo Cruz Foundation, 4365 Manguinhos, Rio de Janeiro 21045-900, Brazil*
[d]*Laboratório de Virologia Molecular-LVM-IOC/FIOCRUZ/Rio de Janeiro-RJ-Brasil, CEP 21041-210, Brazil*
[e]*Instituto de Microbiologia Paulo de Góes, Universidade Federal do Rio de Janeiro, Rio de Janeiro, RJ 21941-902, Brazil*
[f]*National University of Kyiv-Mohyla Academy, 2 Skovorody Vul., Kyiv, 04070, Ukraine. E-mail: v.zaytsev@ukma.edu.ua*

to the top-down one.[22–24] Due to facile preparation and promising characteristics, research on CDs has rapidly developed and in the last three years demonstrates high activity with more than 3000 publications per year (according to Scopus). It is obvious that such rapid development in CDs preparation methodology is accompanied by many errors and misconceptions and results even in nomenclature perplexity.[25] Unclear mechanism of nanoparticle formation from molecular precursors stimulates speculative research on the synthesis of poorly characterized carbon nanodots (CNDs) from almost any organic compound.[26–32] Commonly CNDs have small (1–5 nm) particle size and spherical topology, and no obvious graphene nature of the core.[26,33] Contrary, chemistry of the nanoparticles synthesized from carbon macro objects is much clear.[34] Such nanoparticles have an atomically thin graphitic plane (typically <2 nm thick) and much larger lateral dimensions.[35,36] The bandgap of such nanoparticles is size-dependent,[36] and therefore depending on oxygen content they have been called graphene quantum dots (GQDs) or graphene oxide quantum dots (GOQDs). Generally speaking, the top-down approaches facilitate the fabrication of GOQDs with high crystallinity and a relatively intact structure, while the bottom-up approach has resulted in a mixture of various CNDs.[37]

The biomedical application of CDs requires strict control of the particle size, chemical composition, and morphology.[38] These characteristics determine the properties of the nanoparticles such as toxicity, permeability, and stability of the particle suspensions.[39–42] For example, while large GOQDs particles have low cytotoxicity, small CNDs may have the potential of passing through the blood–brain barrier.[43] Also it was demonstrated that CDs prepared in the bottom-up approach from bamboo demonstrate different cytotoxicity and cell permeability depending on the carbonization procedure.[41] Since information on the composition and morphology of CNDs is much less intact it is more appropriate to use better-defined GOQDs for their biomedical application than poorly characterized CNDs.[44,45]

A general approach for the preparation of GOQDs is based on the shredding of different carbon-containing materials such as coal, carbon black, graphite, carbon fibers, fullerenes, *etc.* Exfoliated GO can be chemically shredded to GOQDs with good yield by $W_{18}O_{49}$, $KMnO_4$, $KHSO_5$, and KO_2.[2,12,46,47] Although powerful oxidants showed high efficiency, it is a tedious task to purify the nanoparticles for metal ion impurities,[36] which may cause undesirable phenomena, such as lowered biocompatibility (in some cases, even toxicity), lowered luminescence efficiency or reduced ability as carriers of active substances.[48,49] Therefore, sophisticated purification techniques are required for GOQDs purification.[50]

As an alternative to metal-containing oxidants, water solution of hydrogen peroxide was successfully texted in preparation of GOQDs from GO in the presence of iron ions.[51] Most likely, GOQDs formation emerges from the process of GO radical epoxidation with further hydrolysis of oxirane cycles.[52] Utilization of H_2O_2 in the GOQDs synthesis is a very desirable approach for their biomedical application since it enables the preparation of metal-free nanoparticles. Therefore, further attempts were performed to avoid the utilization of Fenton reaction. Particularly recently it was demonstrated that H_2O_2 can exfoliate GOQDs in the absence of metal ions under solvothermal conditions.[53,54]

Another important aspect in the preparation of GOQDs is their doping with heteroatoms. Doping of carbonaceous nanoparticles with heteroatoms, such as N, P, S, or B, is an effective way to modulate their chemical, electronic, and structural functionalities. Doping of GOQDs generates local defects in the graphene layer and thus delocalized charge.[55] This charge can be a key factor determining cytotoxicity, cellular uptake, and intracellular trafficking of the nanoparticles.[56] Among the different dopants, nitrogen-doped GOQDs (N-GOQDs) have garnered the most interest due to enhanced photoemission and tunable optical properties rendered by the three possible types of N-doping, including pyridinic N, pyrrolic N, and quaternary.[57] Also N-GOQDs exhibit advantages such as good photothermal conversion efficiency and enhanced ability to generate singlet oxygen and superoxide radical anions[58] that can be used in bioimaging and photodynamic therapy.[59]

Nitrogen doping can be performed through post-synthesis processes, for instance, in hydrothermally treating of GOQDs in ammonia solution. Alternatively, heteroatom doping can be achieved during the top-down synthesis of nanoparticles *via* introducing a heteroatom source or directly using dopant-containing oxidant or reductant.[60]

The current research is devoted to the one-step preparation of green-photoluminescent nitrogen-doped graphene oxide quantum dots (N-GOQDs) having 35 ± 10 nm in lateral size and 1–1.5 nm of height under hydrothermal treatment from graphene oxide in green metal-free and acid-free conditions with a yield of about 100%. For the preparation of N-doped GOQDs, the combination of H_2O_2 as an oxidizer and NH_3 as a dopant seems to be a promising technique. It seems the presence of ammonium in the solution leads to the control of the oxidative potential of hydrogen peroxide and, thus, affects robust the yield of large N-GOQDs. The approach is suitable for the preparation of re-dispersible non-cytotoxic nanoparticles giving indefinitely stable suspensions in saline solution. One-step purification method that allows the separation of N-GOQDs from other carbonaceous residuals was also developed.

2 Materials and methods

2.1. Chemicals and equipment

Potassium permanganate (99%), Triton X-100, methylthiazolyldiphenyl-tetrazolium bromide (MTT), M199 media, dimethyl sulfoxide (DMSO), hydrogen peroxide (30%), and ammonia (33%) solutions were purchased from Sigma-Aldrich. Phosphoric acid (85%), sulfuric acid (95–98%), hydrochloric acid (37%), and sodium hydroxide (97%) were purchased from Vetec (Brazil), while graphite powder came from **https://Synth.com.br** (Brazil). Dialysis membrane (CE MWCO 8000–10 000) from Spectra/Por® Biotech (USA), PTFE filters (0.45 μm) from Sartorius Stedim Biotech (Germany), and filters for syringes (PTFE-hydrophilic with polypropylene pre-filter, 0.22 μm) from Analitica (Brazil) were used for GO and

N-GOQDs purification together with Amicon® stirred cell 50 mL (Sigma-Aldrich) and ultracentrifuge NT800 from Novatecnica (Brazil).

All aqueous solutions were prepared using ultra-pure water obtained on PURELAB Classic, (Elga, UK). Values of pH were measured using a PHS-3E pH-meter with a BioTrode (Hamilton, USA) ion-selective electrode. The electrical conductivities of the suspensions were measured using an HI 8633 conductivity meter (Hanna Instruments, UK). The concentrations of manganese ions in the solution were determined by an Optima 7300 DV inductively coupled plasma optical emission spectrometer (PerkinElmer, USA). Photoluminescence measurements of water suspensions were performed using an LS 55 luminescence spectrometer (PerkinElmer, USA). UV-VIS absorption spectra were measured on a Cary 100 spectrophotometer (Agilent, USA).

The cytotoxicity tests were performed on Vero cell line from the kidney tissue of African green monkey purchased from ATCC (Vero CCL-81™) for pre-sterilized in an autoclave (t = 121 °C, 20 min) suspensions of nanoparticles. The cytotoxicity test was carried out by the MTT method, as described by Mosmann,[61] and the reading was performed using EZ Read 400 ELISA microplate reader (Biochrom, UK).

2.2. Characterization techniques

Atomic force microscopy (AFM) images were obtained using a Bruker MultiMode 8 microscope. A Si tip with a force constant of 0.4 N m^{-1} and a resonance frequency of 70 kHz was used in the tapping peak force method. The samples were diluted in deionized water, ultrasonicated, and dripped on a clean mica surface which then was dried in a nitrogen flux for 2 h. Statistical analysis of the thickness distribution was performed using Gwyddion 2.53 software. The chemical composition of the nanomaterials was investigated from the samples supported on a silicon wafer using X-ray photoelectron spectroscopic (XPS) measurements on high vacuum ESCAplus P System from Omicron Nanotechnology (Germany) with a non-monochromatic Al X-ray source (Kα = 1486.7 eV). The scan-type spectra (survey) were acquired in the range of 1100–0 eV with a step of 1.0 eV, the acquisition time of 0.3 eV, and an analyzer power step of 160 eV. High-resolution spectra were collected for the carbon line, using the analyzer's energy step of 30 eV. The peak fitting was performed using Casa XPS software.

The morphological characteristics of the nanoscale objects were studied by scanning electron microscopy (SEM) in an FEI Magellan 400 microscope applying 20 kV and 100 pA. For these analyses, the sample was sonicated for 30 min and then 1 drop was placed on the silicon wafer and dried under ambient conditions. Transmission electron microscopy (TEM) analysis was performed in a probe-corrected FEI Titan 80-300 apparatus. An X-ray energy dispersive spectroscopy (EDS) detector was used in elemental analysis. The tip-enhanced Raman spectroscopy (TERS) analyses of this work were performed in a bottom illumination TERS system.[62,63] The system is composed of an inverted microscope, a homemade shear-force AFM scan head and a spectrometer (Andor, Shamrock 303i) equipped with a 600 L mm^{-1} grating blazed at 500 nm and a CCD camera (iDUS −70 °C). A radially polarized HeNe laser beam (λ = 632.8 nm) is focused on the bottom of a glass coverslip substrate using an oil immersion 1.4 NA objective. On the other side of the substrate, an optical nanoantenna is positioned around 5 nm from the sample. The nanoantenna used is a plasmon-tunable tip pyramid (PTTP), which shows high optically efficiency and is fabricated by a fully reproducible method.[64–66] The scattered field is collected by the same objective passes throughout a low-pass filter that removes the Rayleigh component and is finally detected at the spectrometer. For the TERS hyperspectral image acquisition of Fig. 9, the laser power at the sample was set to 170 μW, and the image pixel size was 20 nm, with an integration time of 1.0 s.

Dynamic light scattering analyses of 0.6 mg mL^{-1} aqueous N-GOQDs solutions were performed on a nanoparticle analyzer (Horiba SZ-100), equipped with a diode-pumped frequency double laser (532 nm, 10 mW). All measurements were performed by triplicate in standard square optical-glass cells at a scattering angle of 173° (backscattering) and 25 °C.

2.3. Synthesis of graphene oxide (GO)

GO samples were prepared according to the previously reported procedure.[67] In brief, 200 mL of a mixture of concentrated H_2SO_4 and H_3PO_4 (9 : 1 v/v) was added to graphite powder (1.5 g) in a 500 mL round-bottom flask equipped with a mechanical stir bar. Then $KMnO_4$ (9 g) was added slowly at room temperature under stirring and after the flask was heated to 50 °C and kept at this temperature for 12 h. The obtained light-pink mixture was cooled down and poured slowly onto ice (400 mL) with 30% H_2O_2 (20 mL) giving an orange suspension. To remove manganese impurities, the precipitate was separated by centrifugation and washed with HCl (2%). The procedure was repeated until the negative result on Mn impurity in solution was confirmed by Inductively Coupled Plasma Optical Emission Spectroscopy (ICP-OES). Finally, the aqueous suspension of graphene oxide was purified from water-soluble components by dialysis (48 h, membrane 8000–10 000 Da), concentrated on Amicon stirred cell using 0.45 μm PTFE filter, washed with ethanol (3 times) and ether, and dried in vacuum, giving 1.3 g (87%) of fine semi-transparent dark-brown flakes.

2.4. Synthesis of N-GOQDs

To a dispersion of GO (60 mg) in deionized water (20 mL) 1.5 mL of ammonia solution (25%) and 3.0 mL of H_2O_2 (30% solution) were added. The dispersion volume was equalized to 80 mL. The sample was processed under hydrothermal conditions at 180 °C for 2–8 hours (corresponding nanoparticles were denoted as N-GOQDs-n, where n = 2, 4, or 8) in a Teflon cylinder reactor, cooled naturally, and centrifuged at 15 000 rpm (37 000g) for 10 min collecting supernatant. To remove residual non-reacted ammonia and hydrogen peroxide, the green-luminescent water suspension of raw N-GOQDs was lyophilized in vacuum at room temperature resulting in 60 mg of dark-brown non-fluorescent fine powder.

2.5. Purification of N-GOQDs

40 mg of lyophilized powder has been re-dispersed in 50 mL of deionized water and the suspension was filtrated using Millipore Amicon ultrafiltration system employing a hydrophilic 0.22 μm membrane resulting in the preparation of a brawn-yellow suspension containing 40 mg (100% yield) of raw N-GOQDs with green photoluminescence. The aqueous suspension of N-GOQDs was purified from water-soluble components by dialysis (48 h, membrane 8000–10 000 Da). Finally, 0.045 g of NaCl was added to 5 mL of the suspension and stirred on vortex until complete NaCl dissolution. After about 12 h of storage at 4 °C yellow supernatant containing N-GOQDs was separated from a small amount of black precipitate by centrifugation (5 min, 3600 rpm).

2.6. The cytotoxicity tests on the GOQDs

The cytotoxicity effect of N-GOQDs was studied for Vero cell line cultivated in the M199 media. The stock suspension of N-GOQDs (0.57 mg mL^{-1}) was used after gradual dilution (1 : 10, 1 : 100, 1 : 10^3). The MTT salt was reconstituted in sterile phosphate-buffered saline (PBS) at pH 7.2 at a concentration of 5 mg mL^{-1}. For the kinetics studies, the incubation of the cells with N-GOQDs was performed for 3, 6, 24, and 72 hours at 37 °C and 5% CO_2. Additionally, positive control, PC (the cultivated cells only), and negative control, NC (the cells in the presence of Triton X-100) were prepared as references. After incubation, MTT solution was added, and incubation was performed for 2 h. Next, the MTT excess was washed out with 100 μL DMSO and the absorbance of the cell treated with MTT was measured at $\lambda = 570$ nm. To assess the viability of the cells and possible significant differences from the controls, statistical treatment was performed. The normality of the variances was analyzed with the Shapiro–Wilk method to test H_o (normal distribution at $p > \alpha = 0.05$).

3 Results

3.1. GO preparation

GO nanosheets were prepared in a one-step ultrasonic synthesis by oxidation of graphite flakes with $KMnO_4$ in a mixture of concentrated H_2SO_4 and H_3PO_4. It is important to obtain a metal-free GO since even traces of electrocatalytically active metal ions such as Mn^{2+} can essentially alter the procedure of N-GOQDs preparation. To ensure the Mn-free composition of GO samples, the concentration of Mn ions in supernatant solution was monitored using ICP-OES. It is also important to obtain GO with a minimum number of graphitic layers. Contrary to graphene, GO has various polar groups that firmly bind water molecules. To remove water adsorbed between GO layers it was gradually replaced with less polar and more volatile solvents. Following this approach, water suspension of GO was consequently treated with ethanol and diethyl ether and finally dried in a vacuum at room temperature. Obtained under such procedure samples of GO come out in a form of very light translucent brown flakes that can be seen in optical microscopy as transparent sheets, Fig. 1a. Scanning electron microscopy verifies non-porous morphology of the resulted product while AFM microscopy demonstrates 2D morphology of the flakes with thickness below 6 nm, confirming the preparation of few-layer GO, Fig. 1b and c.

3.2. N-GOQDs preparation

The purpose of this research was to develop the procedure of preparation and purification of N-GOQDs suitable for biomedical applications and thus to avoid the utilization of metal-containing oxidative agents due to difficulties related to their separation from the resulted nanoparticles. Therefore, water solution of H_2O_2 and ammonia has been used in the current as shredding agents for the preparation of N-GOQDs from GO under hydrothermal conditions. Shredding efficiency and thus yield of N-GOQDs depends both on the redox potential of the oxidant and the stability of GO. It was assumed that π–π stacking between graphitic layers in GO decreases the internal energy of multilayered GO. Thus shredding of multilayer GO requires utilization of strong metal-containing oxidative agents while few-layer GO can be etched even with H_2O_2.[52] Indeed, by hydrothermal treatment of few-layer GO having only 2–5 nm of the flake thickness (Fig. 1c) N-GOQDs were obtained by hydrothermal treatment of H_2O_2 and ammonia with about 100% yield. The brown-yellow suspension obtained after such treatment did not contain visible amounts of precursor (GO) or other large particles that could be separated by micro-filtration or by high-speed centrifugation.

UV-VIS spectrum of raw N-GOQDs in water demonstrates typical for GOQDs profile – gradually decrease strong absorption in UV-range with shoulders at 340 nm and 480 nm. In addition to the mentioned bands, the spectrum shows very

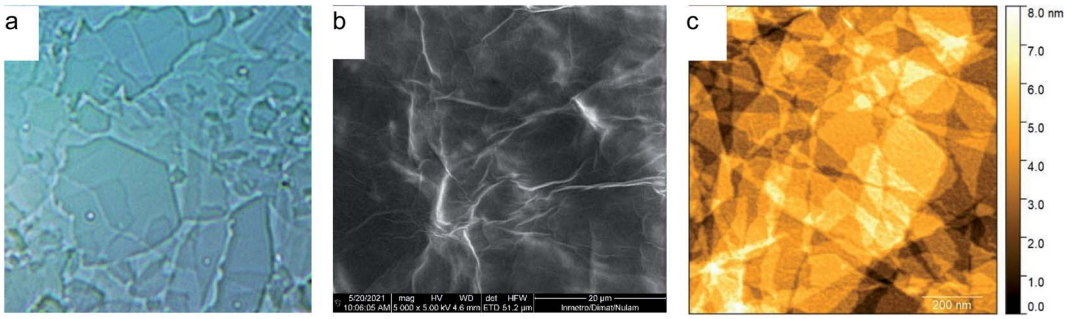

Fig. 1 Images of GO samples in (a) optical (×400), (b) scanning electron, and (c) atomic force microscopies.

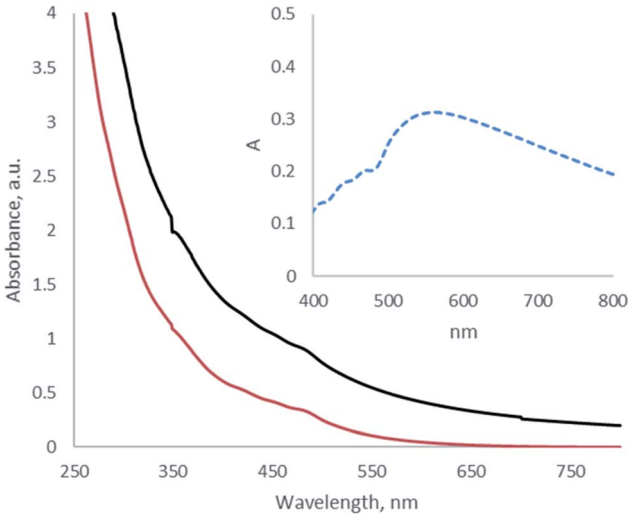

Fig. 2 UV-VIS spectra of as-prepared N-GOQDs in water (black line) and 0.9 wt% NaCl solution (red line), and differential absorption spectrum (inset).

broad absorption below 550 nm, Fig. 2 (inset). This absorption, which contributes to the brown color of the suspension, did not discuss in the literature, but can be attributed to contamination of N-GOQDs by other particles (for example, reduced GOQDs).

It was demonstrated that N-GOQDs can be separated from such impurities by their coagulation in NaCl solution. The addition of solid NaCl to the suspension of raw N-GOQDs precipitates a small amount of black non-luminescent powder, that can be easily separated from yellow supernatant by centrifugation. Suspension of N-GOQDs demonstrates indefinite colloidal stability in physiological solution: no notable changes in UV-VIS spectra were detected during four months of the suspension storage at 4 °C. This enables the biomedical application of N-GOQDs.

3.3. The particles characterization

3.3.1. X-ray photoelectron spectroscopy. The chemical composition of N-GOQDs was determined from energy-dispersive X-ray spectroscopy (EDX), X-ray photoelectron spectroscopy (XPS), and tip-enhanced Raman spectroscopy (TERS). EDX, as well as XPS data, confirms the metal-free nature of the nanoparticles. The full-range XPS spectrum of N-GOQDs shows peaks of N 1s at 401 eV, C 1s at 285 eV, and O 1s at 532 eV confirming obtaining nitrogen doping carbonaceous nanoparticles, Fig. 3a.

According to XPS data, the nanoparticles have a higher content of electronegative atoms (O and N) than parent GO. An increase in the synthesis time amplifies the content of heteroatoms in N-GOQDs from 39.9% (for two-hour synthesis) to 49.1% (for eight-hour synthesis), Table 1. While the content of oxygen increases proportionally with the time of the synthesis, nitrogen doping has a superior limit of 7.2% reached within four hours of synthesis, Table 1.

To understand these phenomena, the high-resolution XPS of N-GOQDs has been studied. The C 1s spectra of N-GOQDs-2 show a peak with essential asymmetry, which allows its convolution to Gaussian peaks at 284.5, 286.2, and 288.1 eV, Fig. 3b. These results suggest that N-GOQDs obtained in two hours of synthesis mainly consist of graphene core with sp^2 carbon atoms and C–N/C–O, and >C=O fragments.[68] For N-GOQDs-4 peak intensity at 286.2 eV augments, indicating the formation of more defects C–N or C–O defects on graphene sp^2 core. Together with this, widening of the peak at 284.5 eV can be observed, indicating the possible formation of C sp^3 moieties. Also, the peak with a maximum at 288.1 eV receives a high energy tail, signifying the formation of some carboxylic (O–C=

Table 1 The atomic composition of graphene oxide (GO) and graphene oxide quantum dots (N-GOQDs), calculated from XPS spectra of the nanoparticles obtained from GO in 2, 4, and 8 hours of synthesis

	Atomic composition (at%)		
Sample	C	O	N
GO	66.4	33.6	<0.1
N-GOQDs-2	60.1	34.6	5.3
N-GOQDs-4	53.1	39.8	7.2
N-GOQDs-8	50.9	45.3	3.8

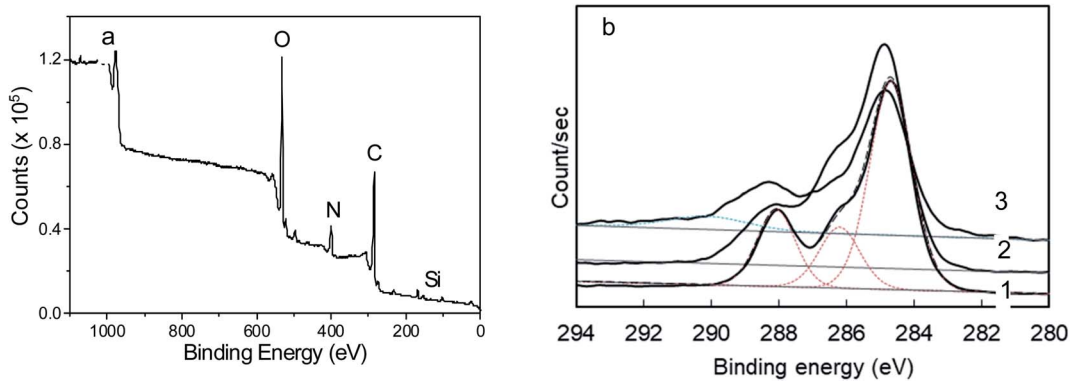

Fig. 3 XPS spectra of N-GOQDs: (a) full-range XPS spectrum, (b) C 1s XPS spectrum of N-GOQDs obtained after two (1), four (2), and eight (3) hours of hydrothermal synthesis. Deconvoluted peaks are indicated by the dash lines.

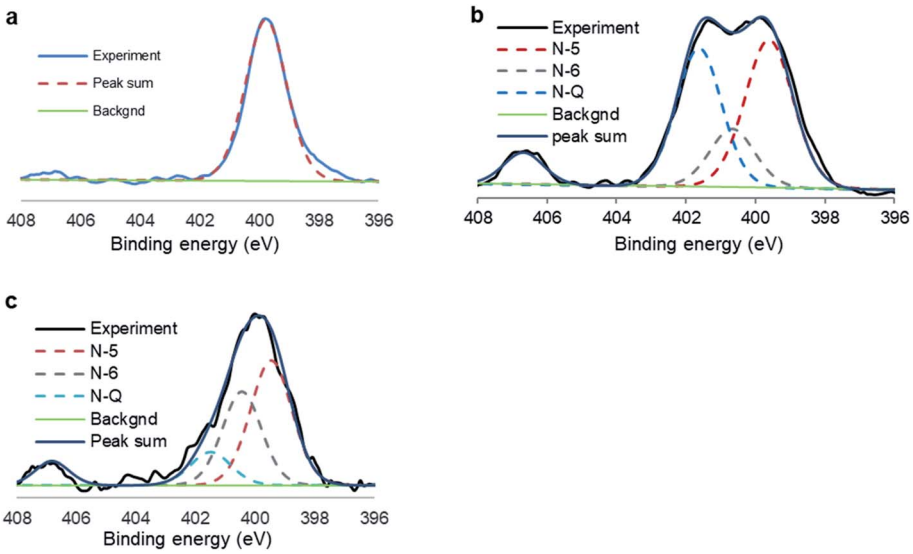

Fig. 4 N 1s XPS spectra of N-GOQDs obtained after two (a), four (b), and eight (c) hours of hydrothermal synthesis. Deconvoluted peaks are indicated by the dash lines.

O) moieties.[68] XPS C 1s spectrum of the nanoparticles obtained in 8 h synthesis exhibits an essentially larger high-energy tail for the peak with a maximum at 288.1 eV and essentially less intensive peak at 286.2 eV, suggesting the further formation of O–C=O fragments for N-GOQDs-8 nanoparticles with simultaneous decreasing of C–N or C–O moieties, Fig. 3b. The only XPS of GOQDs-8 shows a peak at 291 eV that can be attributed to shakeup satellites, indicating $\pi \rightarrow \pi^*$ type transitions in graphene core.[69]

The N 1s XPS spectra of N-GOQDs have different appearances depending on the time of the nanoparticle synthesis, Fig. 4. XPS for N-GOQDs-2 shows a symmetrical peak at 399.8 eV being attributed to $(C)_2$–NH (denoted as N-5, Fig. 5) bonding, and a very weak peak at 406.7 eV. The spectrum of N-GOQDs-4 particles is deconvoluted into four peaks named N-5, N-6, N-Q, and N-X and their binding energy was constrained at 399.8, 400.6, 401.5, and 406.7 eV respectively.[70] The N-6 peak is attributed to pyridinic nitrogen where a nitrogen atom substitutes for a carbon atom in an aromatic ring. The N-5 peak is related to organic nitrogen in pyrrolic derivatives and the nitrogen atom is just bonded to one hydrogen atom and two carbon atoms, amine, and amide. The N-Q peak is associated with quaternary nitrogen where the nitrogen atom substitutes the carbon atom in a condensed aromatic ring system and each nitrogen is bonded to three carbon atoms. The N-X peak is usually assigned to the pyridinic *N*-oxide (Fig. 4).[70]

The functional composition of N-GOQDs estimated from the results of C 1s and N 1s XPS spectra is presented in Table 2.

From C 1s XPS data of N-GOQDs, it can be concluded that the nanoparticles obtained in two hours of synthesis consist of graphene core (62%) modified with C–N/C–O (18%) and >C=O (20%) moieties. With increasing the synthesis time graphene fraction is slightly reduced, while loading of lateral carboxylic groups rises to 9% of the total carbon content, Table 2. The XPS N 1s data demonstrate essential changes in the speciation of nitrogen for different N-GOQDs. The particles obtained in two hours of synthesis contain only N-5 moieties, while those

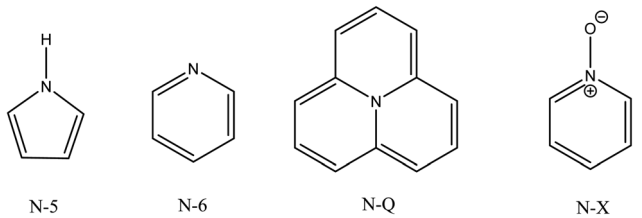

Fig. 5 Schematic nitrogen-containing molecular structures.

Table 2 The relative area of the peaks obtained by deconvolution of C 1s and N 1s high-resolution XPS of N-GOQDs

	Relative peak area (%)				
	Carbon				
Sample	C=C	C–N and C–O	C=O	O–C=O	π–π*
N-GOQDs-2	62	18	20	0	0
N-GOQDs-4	57	26	13	5	0
N-GOQDs-8[a]	58	18	15	9	9

	Nitrogen			
Sample	N-5	N-6	N-Q	N-X
N-GOQDs-2	100	0	0	0
N-GOQDs-4	41.2	15.2	36.2	7.4
N-GOQDs-8	47.2	33	12.3	7.5

[a] Calculated without considering π–π* band.

prepared for a longer time have above 50% of other nitrogen-containing functional fragments, Table 2. Pyridine derivatives are much more stable to H_2O_2 treatment than N-5 and N-Q sites, therefore a fraction of N-6 moieties grows with the time of synthesis, while N-Q declines. Also, only N-6 fragments can react with H_2O_2 giving pyridine *N*-oxide derivatives. Thus, according to XPS quantitative analysis, N-GOQDs-8 can have up to 40.5% of the total nitrogen loading in form of pyridine derivatives, part of which (7.5%) can be in form of *N*-oxide (N-X sites), Table 2.

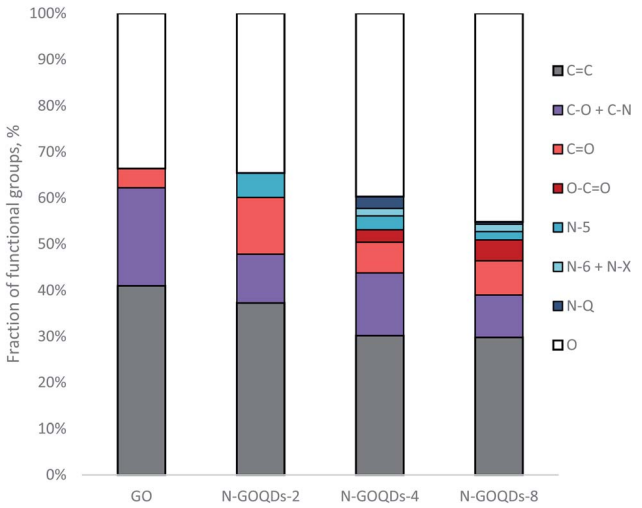

Fig. 6 Relative functional composition of N-GOQDs obtained in two (N-GOQDs-2), four (N-GOQDs-2), and eight (N-GOQDs-2) hours of the hydrothermal synthesis.

Taking to account the atomic content of N-GOQDs (Table 1) and the results of C 1s and N 1s XPS quantification (Table 2), the overall functional composition of the nanoparticles obtained in different experimental conditions has been determined. From the results presented in Fig. 6, it can be seen that increasing the time of N-GOQDs synthesis leads to gradual oxidation of the graphene layer and partial elimination of nitrogen moieties. In contrast, the fraction of lateral carboxylic groups increases with time.

3.3.2. Tip-enhanced Raman spectroscopy. Raman spectroscopy is one of the most powerful techniques to study graphite and graphene systems, although its spatial resolution is diffraction-limited to around 300 nm. On the other hand, TERS can overcome the diffraction limit by applying an optical nanoantenna to make use of the near-field information.[64] In Fig. 7, we applied TERS analyses using a high optically efficient PTTP nanoantenna to locally investigate the Raman response of the N-GOQDs with a resolution up to 20 nm.[64,71] Fig. 7a shows a hyperspectral image where the blue-to-white color scale renders the Raman G band intensity. This optical image can be compared to the topography image (Fig. 7b) simultaneously acquired with the nano-Raman image, from which five big nanoparticles within 50 nm to 150 nm of lateral size, and 10 nm to 25 nm of height, can be observed surrounded by a lot of small nanoparticles with a lateral size smaller than 30 nm and around 1 nm of height. The bigger ones are possibly clusters of N-GOQDs and their spectra are plotted in greyscale in the graph

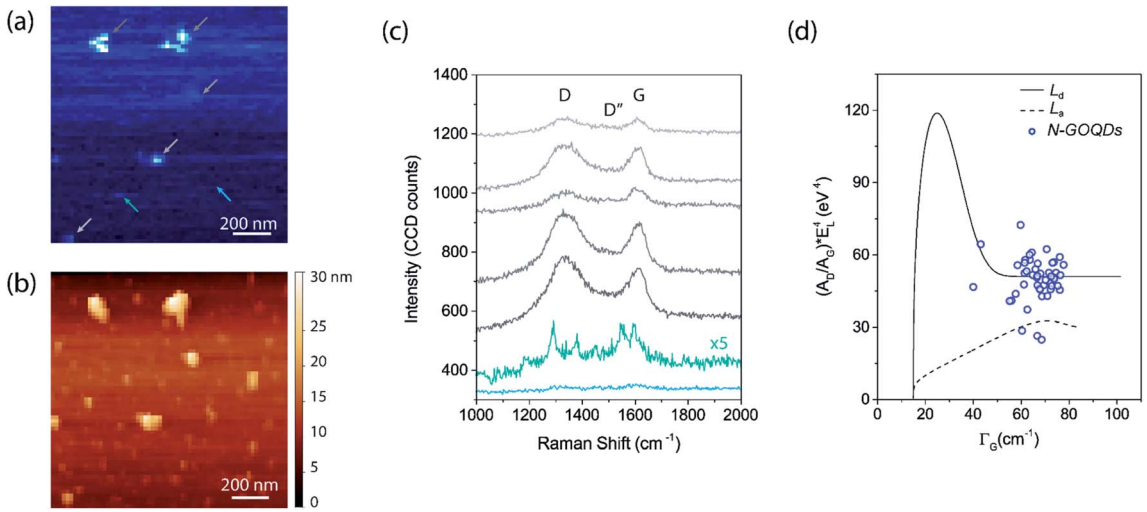

Fig. 7 TERS analysis of N-GOQDs nanoparticles at glass coverslip substrate. (a) TERS hyperspectral image with a pixel size of 20 nm, blueish color rendering the G band. (b) Topography image simultaneously collected with the nano-Raman imaging, showing nanoparticles with a lateral size smaller than 50 nm well dispersed over the substrate and a few bigger nanoparticles agglomeration of around 100 nm. (c) TERS spectra were collected at pixel positions indicated by the arrows on image (a), where the grey color arrows with five distinct brightness are from the biggest nanoparticles, whereas the green and blue were collected elsewhere, indicating the optical information from the substrate (blue) and at a single N-GOQDs nanoparticle (green). All spectra were shifted, and the green spectrum was multiplied 5 times to clarity. (d) Scatter plot of the $(A_D/A_G) \times E_{laser}^4$ as function of the G band's linewidth (Γ_G) from the data over the five biggest agglomerated nanoparticles. The black dashed and solid curves were adapted from the study of the influence of defects on the Raman spectra of graphene.[74] The dashed curve was calculated for varying the average distance between nearest defects (L_D) and considering a fixed value of the graphene average crystallite size $L_A = 500$ nm. This solid curve was calculated for different values of L_A, with L_D fixed at 500 nm.

(Fig. 7c), showing in all plots the same defect-like graphene behavior for the disorder-induced D band (~1340 cm^{-1}) and the first order allowed bond-stretching G band (~1600 cm^{-1}). Another less intense peak at around ~1520 cm^{-1} (D″ band) was observed with D″/G ~ 0.3, as conventionally reported for graphene oxide samples.[72] In addition, two spectra were plotted in the graph in color (Fig. 7c): the green spectrum was collected out from a very small nanoparticle (probably a single N-GOQD), and the blue one, was obtained from the substrate with low-intensity of D and G peaks can be assigned to the far-field contribution. Interestingly, the spectra collected on a single N-GOQD (green) shows five narrow peaks at 1291 cm^{-1}, 1380 cm^{-1}, 1448 cm^{-1}, 1548 cm^{-1} and 1600 cm^{-1}. This can be evidence of molecular size GO nanoparticle, for which its Raman peaks are expected to be shifted and narrowed, as well as new peaks, that can be observed as a result of electron and phonon lateral confinement.[73]

Also, the intensity of the D and G bands and the width of the G band can be used to estimate the density of defects and the graphene crystallite size.[72] To do so, we plotted in the graph (Fig. 9d) the data from the spectra acquired on the bigger nanoparticles. The graph shows the calculated $(A_D/A_G) \times {E_{laser}}^4$ as function of the G band linewidth Γ_G, where E_{laser} is the energy of the laser used, which in our case is 1.96 eV, A_D and A_G are the area of the D and G peaks, calculated by fitting on the data three Lorentzian curves for the D (1336 cm^{-1}), G (1605 cm^{-1}) and D′ (1620 cm^{-1}) peaks, and one Gaussian curve for the D″ (1523 cm^{-1}) peak. In the same graph, we included two curves adapted from the work of ref. 74. As better described in this referenced work, the dashed curve was calculated for varying the average distance between nearest defects (L_D) and considering a fixed value of the graphene average crystallite size $L_A = 500$ nm, whereas the black solid curve was calculated for different values of L_A with fixed $L_D = 500$ nm. By comparing our data, with mean values of $(A_D/A_G) \times {E_{laser}}^4 = 50$ eV^4 and $\Gamma_G = 66$ cm^{-1}, to the data from ref. 74 we can assume that the N-GOQDs show graphene crystallite size of around 9 nm and L_D smaller than 3 nm. These values found corroborates with the expected for a disorder carbon of N-GOQDs, even when considering the TERS effect on this methodology made for micro-Raman, which leads to a correction factor that would reduce the contribution of $(A_D/A_G) \times {E_{laser}}^4$, and thus improving the L_D value for a few nanometers, as shown in the work of ref. 75.

Considering GO model proposed by Rourke[76] and further developed by Hassenkam,[77] the functional structure of N-GOQDs was proposed. The structure matches the results of the chemical analysis of the corresponding particles. Nitrogen dopants are mainly allocated in the graphene basal plane, while oxygen ones are on the particle edges, Fig. 8. It can be seen that different nitrogen sites of N-GOQDs generate different kinds of defects. Because the fractions of the sites depend on the particles' preparation conditions (Fig. 6), variation of such conditions can result in changing of optical and biomedical properties of the N-GOQDs. Also, the structure demonstrates heavy carboxylation of the particle edges, which explains experimentally observed high stability of the particle in water suspension and physiological solution. These observations can be useful to design N-GOQDs with specific functionality.

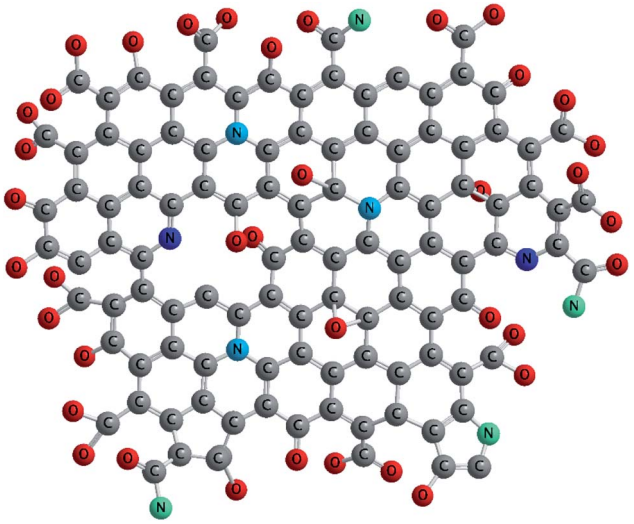

Fig. 8 Schematical presentation of N-GOQDs-4.

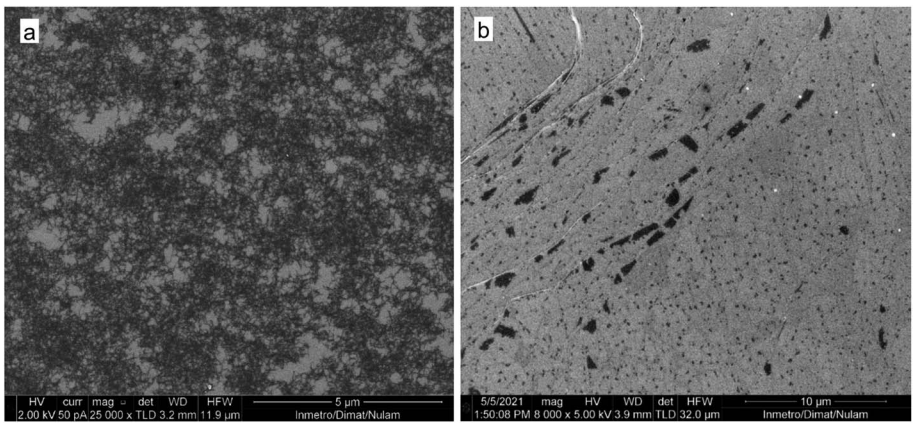

Fig. 9 SEM images of the precipitate obtained by treatment of water suspension of raw N-GOQDs with 0.9 mL NaCl solution (a) and remaining supernatant (b).

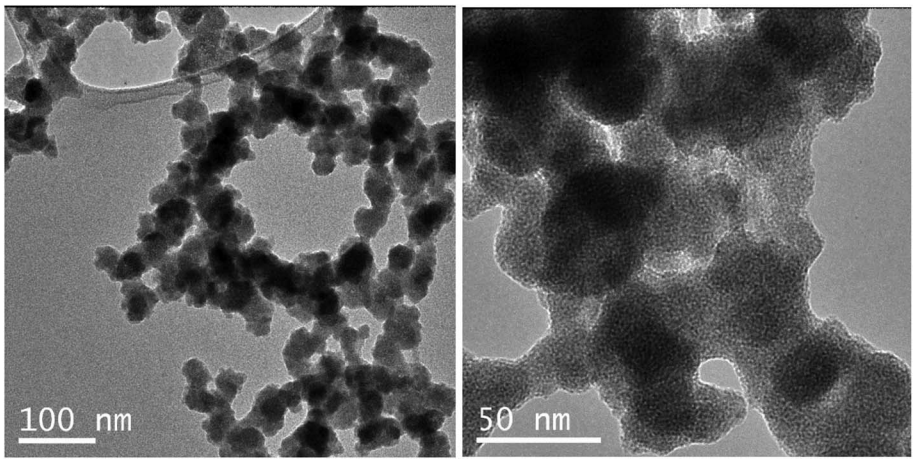

Fig. 10 TEM image of N-GOQDs-8 obtained by hydrothermal treatment of GO with H_2O_2 and NH_3.

3.3.3. Electron microscopy. As it was mentioned in Section 3.2, raw N-GOQDs are contaminated by other carbonaceous residuals that coagulate in physiological solution. SEM image of this coagulate presented in Fig. 9a demonstrates that this precipitate forms the network, which possibly represents the remains of GO after chemical etching of N-GOQDs. N-GOQDs demonstrate stability in physiological solution and thus can be easily separated from the impurities. SEM image of N-GOQDs on silicon wafer presented in Fig. 9b.

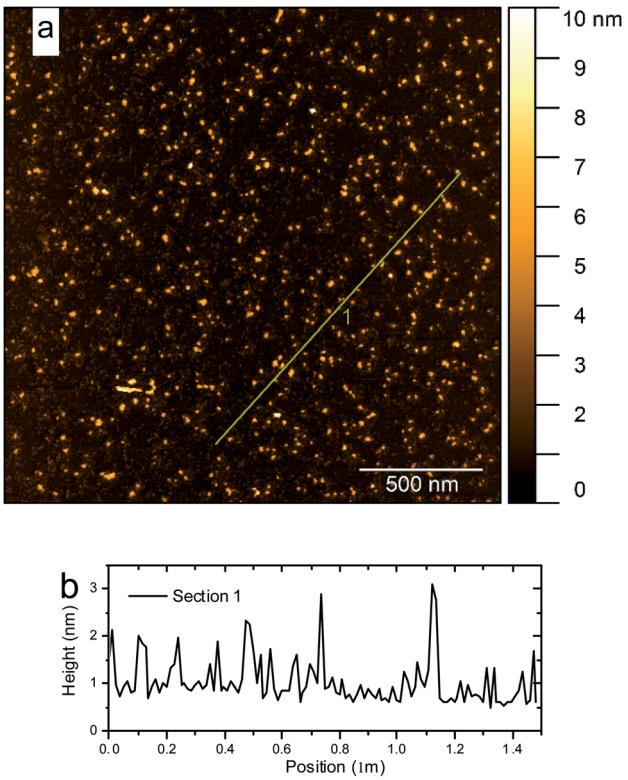

Fig. 11 AFM images of the GOQDs (a) with their height profile along the line marked in the AFM image (b).

According to the result of TEM, N-GOQDs obtained in the current research have an irregular shape with an average lateral size of about 35 ± 10 nm, Fig. 10.

3.3.4. Atomic force microscopy. AFM image of N-GOQDs nanoparticle adsorbed on mica substrate demonstrates that the height of the nanoparticles does not exceed 1.0–1.5 nm, Fig. 11. Variations in lateral size and topology of the N-GOQDs can also be seen from the AFM image. The investigation demonstrates that the N-GOQDs have an irregular shape, they are significantly larger but essentially thinner than CNDs.[26] Irregular shape of N-GOQDs particles also logically follows from the mechanism of their formation by chemical shredding of GO. Such difference can be very important in the biomedical application of N-GOQDs, particularly in their cytotoxicity and cell essential changes.

3.3.5. Dynamic light scattering. Suspension of N-GOQDs in water is very stable and thus allows investigation by dynamic light scattering (DLS) method, for determination of the hydrodynamic diameter of the particles. This parameter is more important for biomedical applications of the N-GOQDs than the particle size determined by TEM. As it can be seen from the data presented, raw N-GOQDs demonstrate the large asymmetric distribution of their hydrated size in the frame of 40–500 nm (Fig. 12a), while purified by coagulation of impurities in NaCl show much narrow particle size distribution between 50 and 120 nm (Fig. 12b). These results indicate the need for nanoparticles purification before their biomedical utilization.

3.4. Spectroscopic and photoluminescent properties of N-GOQDs

As-prepared N-GOQDs can be dried in a vacuum and then redispersed in water by vortex shaking or under ultrasound treatment. This action does not affect the UV-VIS spectra of N-GOQDs suspensions in water, reducing insignificantly (10–15%) the absorption intensity of the suspensions in a wide range of the nanoparticle concentration (from 2×10^{-1} g L^{-1}), Fig. 13.

Due to essential variation in the particle size and chemical composition, samples of N-GOQDs demonstrate excitation-

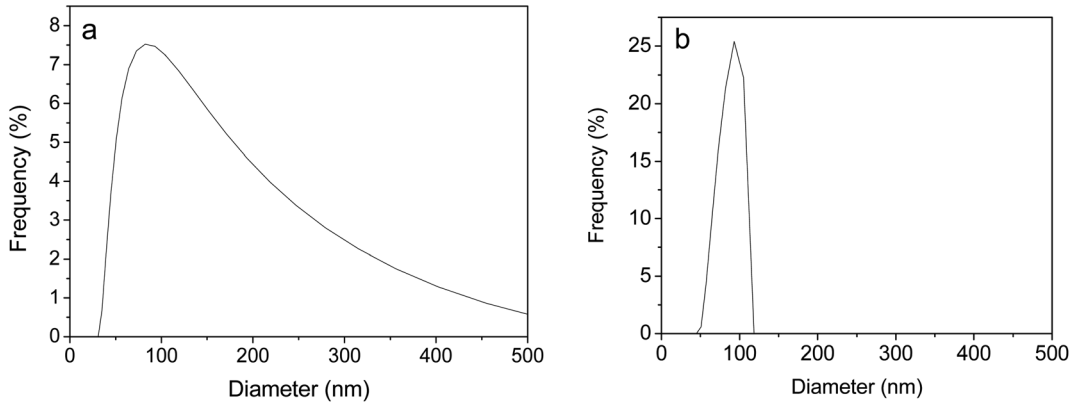

Fig. 12 Dynamic light scattering of raw N-GOQDs-4 (a) and the same particles after purification with NaCl (b).

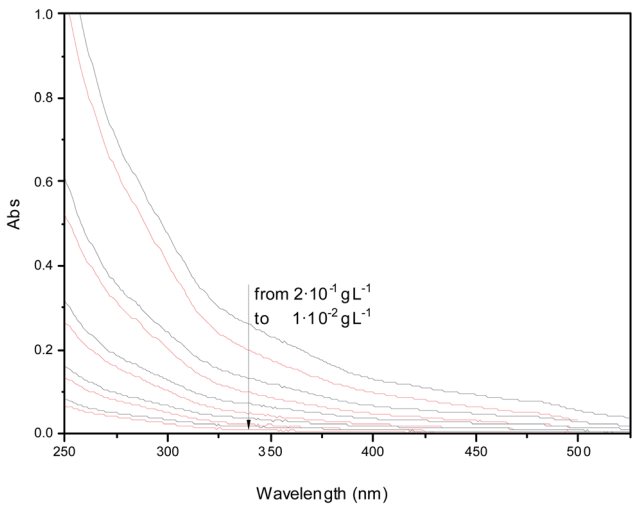

Fig. 13 UV-VIS absorption spectra of water suspensions obtained at different concentrations of as-prepared (black lines) and re-dispersed (red lines) N-GOQDs.

dependent photoluminescence, Fig. 14a. Photoemission at 460–520 nm can be successfully exited by visible light from 390 to 480 nm. When the N-GOQDs suspension is excited by light with a wavelength less than 430 nm, their photoemission band is wide and asymmetric. With the increase of the exited wavelength, the emission bandwidth decreases from its high-energy wing. At 430 nm of excitation, the emission band reaches its maximum intensity at 500 nm, Fig. 14b.

Unlike UV-Vis spectroscopy, linear correlation between the concentration of N-GOQDs and photoluminescence emission is observed for diluted water suspension of the nanoparticles only, up to 100 mg L^{-1} (Fig. 15) due to the inner filter effect.

3.5. Cytotoxicity of N-GOQDs

First, it was shown that the suspension of N-GOQDs-4 in the M199 culture medium is stable. For this, the suspension luminescence was monitored periodically for 74 h, and no tendency of decrease was detected. Cytotoxicity results demonstrated that the viability of Vero cell line in the presence of N-GOQDs was not significantly lower than for positive control at all experimental conditions for 3, 6, 24, or 72 h of incubation. The significant difference in the comparison of the mean was revealed by negative control (NC) over the full kinetics profile. The saline as a reference was slightly different from the 1 : 100 dilution at 6 h of incubation ($p = 0.0287$, Fig. 16b) and to 1 : 10, 1 : 100 and PC at 24 h of incubation ($p = 0.0074$, 0.0127 and 0.0172, respectively Fig. 16c). In terms of decision-making,

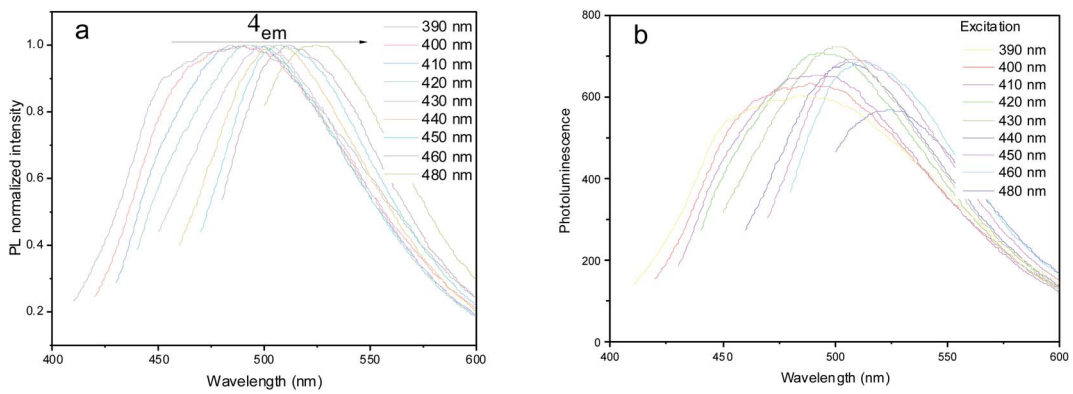

Fig. 14 Normalized (a) and absolute (b) photoluminescence spectra of diluted N-GOQDs water suspension at different excitation wavelengths.

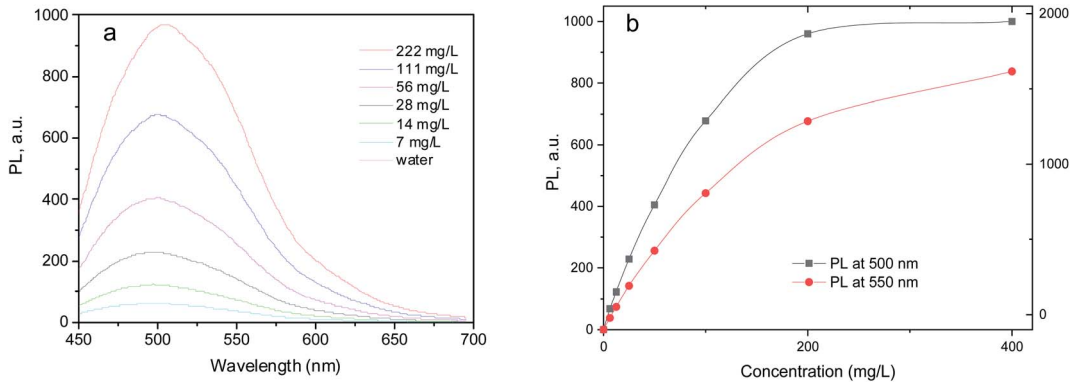

Fig. 15 (a) Photoluminescence spectra of N-GOQDs suspensions in water (excitation wavelength 430 nm); (b) the variation of photoluminescence intensity as a function of N-GOQDs concentration.

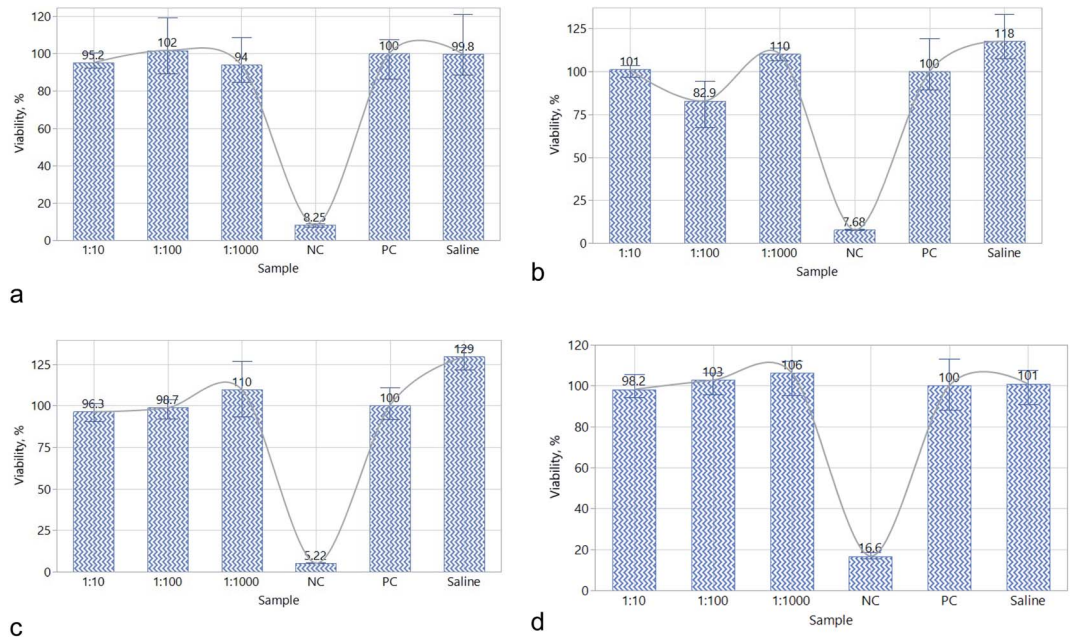

Fig. 16 Viability of cells in sterilized and diluted (D) 10, 100, and 1000 times N-GOQDs sample in culture medium after 3 (a), 6 (b), 24 (c), and 72 (d) hours of treatment.

these values speak that p is not low enough to reject the null hypothesis for the equality of the means.

Because of nomenclature perplexity, the data available on CDs cytotoxicity is very confused. Even in the latest reviews various CDs having different topology, composition and sizes are commonly considered as GQDs,[78–80] which is wrong. It seems small spherical CNDs are less cytotoxic than plane large GQDs, probably due to different permeability and transport mechanisms.[81,82] For example it was demonstrated that the viability of cancer cells (cervical cancer cells HeLa, lung carcinoma cells A549, *etc.*) decreases from 97% to 75% with increasing of CNDs particles size.[83] For GOQDs having a lateral size above 50 nm, the viability of human glioma cells U251 is about 75% at the concentration of nanoparticles 0.1 mg mL^{-1} and incubation period of 24 hours.[84] Other aspect of confusion is perplexity in doping (substation of carbon atoms of the graphene layer by heteroatoms) and functionalization (immobilization of various functional groups on the lateral sides of the particle) of CDs. It was demonstrated that nitrogen-functionalized CNDs are more cytotoxic than carboxylated or oxygenated ones, probably due to differences in surface charge.[85] Contrary to CNDs, nitrogen-doped GQDs demonstrate even higher (over 90%) viability than pristine ones.[83] This research shows that N-GOQDs can demonstrate even smaller cytotoxicity than N-GQDs with the viability of Vera cells up to 98% after 72 hours of incubation in 60 mg L^{-1} of N-GOQDs suspension, Fig. 16. Such effect can be explained by the functional structure of N-GOQDs (Fig. 8): the N-GOQDs are more oxygenated than N-GQDs, and they are heavily carboxylated on the edges. These two factors are in favor to reduce the cytotoxicity of N-GOQDs.[82]

4 Conclusions

It is demonstrated that N-GOQDs can be obtained from few-layer GO under hydrothermal treatment with H_2O_2 and ammonia with a yield of about 100%. The brown-yellow suspension obtained after such treatment did not contain visible amounts of precursor or other large particles that can be separated by micro-filtration or by high-speed centrifugation. Nevertheless, UV-Vis spectra of raw N-GOQDs show a very broad absorption band below 550 nm suggesting high molecular weight impurities that can be removed by coagulation with NaCl solution. Resulted re-dispersible N-GOQDs demonstrate indefinite stability of their suspensions in water and physiological solution. The chemical composition of N-GOQDs determined for XPS and TERS that the procedure proposed allows obtaining nitrogen-doped GOQDs with up to 7.2% of nitrogen. Deconvolution of C 1s peaks in high-resolution XPS allows to demonstrate that N-GOQDs obtained in two hours of synthesis mainly consist of graphene core with 18% of C–N or C–O defects, and about 20% of C=O fragments located on the particle edges. The N-GOQDs obtained in 4–8 hours of hydrothermal treatment show heavy carboxylation of the particle edges. Analysis of high-resolution N 1s XPS allowed proving nitrogen doping of graphene core with formation of N-5, N-Q, N-6, and N-X defects. The fractional composition of nitrogen defects depends on the synthesis time. TEM, AFM, and TERS prove the planar topology of N-GOQDs with about 1.0–1.5 nm of height and 35 ± 10 nm of lateral size. The functional structure of N-GOQDs proposed demonstrates that nitrogen dopants are mainly allocated in the graphene basal plane, while oxygen ones are on the particle edges in form of carboxylic groups that ensure the particle solubility in water and physiological solutions. Due to essential variation in the particle size and chemical composition, samples of N-GOQDs demonstrate excitation-dependent photoluminescence with emission at 460–520 nm that can be excited by visible light. The N-GOQDs have exhibited outstanding compatibility with the monkey epithelial kidney cells (Vero), which are used in COVID-19 research, resulting in almost 100% viability. This fact proves the effectiveness of the applied techniques to prepare stable luminescent dispersions of GOQDs for further relevant uses.

Author contributions

Michael Nazarkovsky – investigation (NP synthesis and purification), formal analysis, writing; Albina Mikhraliieva – investigation (NP synthesis and spectroscopy), writing; Carlos A. Achete – supervision (microscopia, XPS, TERS); Luiz Anastacio Alves – methodology (bioactivity); Joyce Araujo – investigation (microscopia SEM); Bráulio S. Archanjo – investigation (microscopia TEM); Joé Júnior França de Barros – supervision (bioactivity); Liana Monteiro da Fonseca Cardoso – methodology (bioactivity); José Nelson S. S. Couceiro – investigation (bioactivity); Fernanda Davi Marques – investigation (XPS); Bruno S. Oliveira – investigation (TERS, RAMAN); Rafael Nascimento Dias de Souza – investigation (microscopia TEM); Ayla Josma Teixeira – investigation (bioactivity); Thiago L. Vasconcelos – investigation (TERS, RAMAN); Vladimir Zaitsev – conceptualization, supervision (NP synthesis), writing – original draft.

Conflicts of interest

The authors declare no competing financial interest.

Acknowledgements

Authors are grateful for the financial support received from Fundação Carlos Chagas Filho de Amparo à Pesquisa do Estado do Rio de Janeiro (FAPERJ) (grants E-26/010.155/2020, E-26/010.978/2019 and E-26/010.1556/2019). VZ gratefully acknowledges Conselho Nacional de Desenvolvimento Científico e Tecnológico (CNPq) (grants 306992/2018-3, 438450/2018-3) for financial support. TLV acknowledges financial support from Financiadora de Estudos e Projetos (FINEP) (grant SibratecNano 21040). This research used facilities of the Brazilian Nanotechnology National Laboratory (LNNano), part of the Brazilian Centre for Research in Energy and Materials (CNPEM), a private non-profit organization under the supervision of the Brazilian Ministry for Science, Technology, and Innovations (MCTI). The Spectroscopy and Scattering staff of LNNano is acknowledged for their assistance during the experiments (XPS-20220035). The AFM staff of LNNano is acknowledged for their assistance during the experiments (AFM-27716). The authors thank INMETRO and UFMG for the PTTPs nanoantennas used in the TERS experiment. We also acknowledge the help of Ricardo Queiroz Aucélio in obtaining and interpreting fluorescence spectra.

References

1 S. Anwar, H. Ding, M. Xu, X. Hu, Z. Li, J. Wang, L. Liu, L. Jiang, D. Wang, C. Dong, M. Yan, Q. Wang and H. Bi, *ACS Appl. Bio Mater.*, 2019, **2**, 2317–2338.
2 X. Tian and X. Yin, *Small*, 2019, **15**, 1901803.
3 C. Hu, M. Li, J. Qiu and Y.-P. Sun, *Chem. Soc. Rev.*, 2019, **48**, 2315–2337.
4 X. Xu, R. Ray, Y. Gu, H. J. Ploehn, L. Gearheart, K. Raker and W. A. Scrivens, *J. Am. Chem. Soc.*, 2004, **126**, 12736–12737.
5 L. Wang, Y. Wang, T. Xu, H. Liao, C. Yao, Y. Liu, Z. Li, Z. Chen, D. Pan, L. Sun and M. Wu, *Nat. Commun.*, 2014, **5**, 5357.
6 Y. Park, J. Yoo, M.-H. Kang, W. Kwon and J. Joo, *J. Mater. Chem. B*, 2019, **7**, 6271–6292.
7 J. Shamsi, A. S. Urban, M. Imran, L. De Trizio and L. Manna, *Chem. Rev.*, 2019, **119**, 3296–3348.
8 H. Liu, J. Ding, K. Zhang and L. Ding, *TrAC, Trends Anal. Chem.*, 2019, **118**, 315–337.
9 R. Mohammadinejad, A. Dadashzadeh, S. Moghassemi, M. Ashrafizadeh, A. Dehshahri, A. Pardakhty, H. Sassan, S.-M. Sohrevardi and A. Mandegary, *J. Adv. Res.*, 2019, **18**, 81–93.
10 D. T. Omstead, J. Sjoerdsma and B. Bilgicer, *Annu. Rev. Anal. Chem.*, 2019, **12**, 69–88.

11 P. C. Wu, J. Y. Wang, W. L. Wang, C. Y. Chang, C. H. Huang, K. L. Yang, J. C. Chang, C. L. L. Hsu, S. Y. Chen, T. M. Chou and W. S. Kuo, *Nanoscale*, 2018, **10**, 109–117.
12 M. Pirsaheb, S. Mohammadi, A. Salimi and M. Payandeh, *Microchim. Acta*, 2019, **186**, 231.
13 M. K. Kumawat, M. Thakur, R. B. Gurung and R. Srivastava, *Sci. Rep.*, 2017, **7**, 1–16.
14 M. Pirsaheb, S. Mohammadi and A. Salimi, *TrAC, Trends Anal. Chem.*, 2019, **115**, 83–99.
15 Y. Yuan, B. Guo, L. Hao, N. Liu, Y. Lin, W. Guo, X. Li and B. Gu, *Colloids Surf., B*, 2017, **159**, 349–359.
16 K. O. Boakye-Yiadom, S. Kesse, Y. Opoku-Damoah, M. S. Filli, M. Aquib, M. M. B. Joelle, M. A. Farooq, R. Mavlyanova, F. Raza, R. Bavi and B. Wang, *Int. J. Pharm.*, 2019, **564**, 308–317.
17 D. Lu, R. Tao and Z. Wang, *Front. Chem. Sci. Eng.*, 2019, **13**, 310–323.
18 Q. Wang, H. Zheng, Y. Long, L. Zhang, M. Gao and W. Bai, *Carbon*, 2011, **49**, 3134–3140.
19 X. Zhang, S. Wang, C. Zhu, M. Liu, Y. Ji, L. Feng, L. Tao and Y. Wei, *J. Colloid Interface Sci.*, 2013, **397**, 39–44.
20 X. Li, H. Wang, Y. Shimizu, A. Pyatenko, K. Kawaguchi and N. Koshizaki, *Chem. Commun.*, 2011, **47**, 932–934.
21 F. Yuan, L. Ding, Y. Li, X. Li, L. Fan, S. Zhou, D. Fang and S. Yang, *Nanoscale*, 2015, **7**, 11727–11733.
22 S. Zhu, X. Zhao, Y. Song, S. Lu and B. Yang, *Nano Today*, 2016, **11**, 128–132.
23 D. Qu and Z. Sun, *Mater. Chem. Front.*, 2020, **4**, 400–420.
24 S. Shen, J. Wang, Z. Wu, Z. Du, Z. Tang and J. Yang, *Nanomaterials*, 2020, **10**, 375.
25 S. Mandal and P. Das, *Appl. Mater. Today*, 2022, **26**, 101331.
26 A. Mikhraliieva, V. Zaitsev, Y. Xing, H. Coelho-Júnior and R. L. Sommer, *ACS Appl. Nano Mater.*, 2020, **3**, 3652–3664.
27 Z. Song, X. Wang, G. Zhu, Q. Nian, H. Zhou, D. Yang, C. Qin and R. Tang, *Small*, 2015, **11**, 1171–1176.
28 K.-W. Chu, S. Lee, C.-J. Chang and L. Liu, *Polymers*, 2019, **11**, 689.
29 H. Li, Z. Kang, Y. Liu and S. T. Lee, *J. Mater. Chem.*, 2012, **22**, 24230–24253.
30 A. J. G. Afonso, F. T. Aquino, G. M. L. Dalmônico, M. V. Nascimento, E. Wrasse and K. M. F. R. de Aguiar, *Carbon Lett.*, 2022, **32**, 131–141.
31 A. Ghosh and G. Das, *New J. Chem.*, 2021, **45**, 8747–8754.
32 S. Perumal, R. Atchudan, T. N. J. I. Edison and Y. R. Lee, *J. Environ. Chem. Eng.*, 2021, **9**, 105802.
33 A. Cayuela, M. L. Soriano, C. Carrillo-Carrión and M. Valcárcel, *Chem. Commun.*, 2016, **52**, 1311–1326.
34 J. B. Essner, J. A. Kist, L. Polo-Parada and G. A. Baker, *Chem. Mater.*, 2018, **30**, 1878–1887.
35 P. Tian, L. Tang, K. S. Teng and S. P. Lau, *Mater. Today Chem.*, 2018, **10**, 221–258.
36 Y. Yan, J. Gong, J. Chen, Z. Zeng, W. Huang, K. Pu, J. Liu and P. Chen, *Adv. Mater.*, 2019, **31**, 1–22.
37 F. Rigodanza, M. Burian, F. Arcudi, L. Đorđević, H. Amenitsch and M. Prato, *Nat. Commun.*, 2021, **12**, 2640.
38 L. Zhao, L. Zhao, H. Li, J. Ma, L. Bian, X. Wang and Q. Pu, *Talanta*, 2021, **228**, 122224.
39 S. Mani, G. Swargiary, S. Tyagi, M. Singh, N. K. Jha and K. K. Singh, *Life Sci.*, 2021, **281**, 119773.
40 X. Dong, R. Edmondson, F. Yang, Y. Tang, P. Wang, Y.-P. Sun and L. Yang, *RSC Adv.*, 2020, **10**, 33944–33954.
41 Y.-Y. Chen, W.-P. Jiang, H.-L. Chen, H.-C. Huang, G.-J. Huang, H.-M. Chiang, C.-C. Chang, C.-L. Huang and T.-Y. Juang, *RSC Adv.*, 2021, **11**, 16661–16674.
42 T. S. Hauck, R. E. Anderson, H. C. Fischer, S. Newbigging and W. C. W. Chan, *Small*, 2010, **6**, 138–144.
43 Y. Liu, H. Huang, W. Cao, B. Mao, Y. Liu and Z. Kang, *Mater. Chem. Front.*, 2020, **4**, 1586–1613.
44 A. Kasouni, T. Chatzimitakos and C. Stalikas, in *Comprehensive Analytical Chemistry*, 2021, vol. 94, pp. 507–531.
45 A. Rhazouani, H. Gamrani, M. El Achaby, K. Aziz, L. Gebrati, M. S. Uddin and F. Aziz, *BioMed Res. Int.*, 2021, **2021**, 1–19.
46 N. Kottam and S. P. Smrithi, *Methods Appl. Fluoresc.*, 2021, **9**, 012001.
47 S. Tajik, Z. Dourandish, K. Zhang, H. Beitollahi, Q. Van Le, H. W. Jang and M. Shokouhimehr, *RSC Adv.*, 2020, **10**, 15406–15429.
48 X. Hu, X. An and L. Li, *Mater. Sci. Eng., C*, 2016, **58**, 730–736.
49 X. Xu, D. Ren, Y. Chai, X. Cheng, J. Mei, J. Bao, F. Wei, G. Xu, Q. Hu and Y. Cen, *Sens. Actuators, B*, 2019, **298**, 126829.
50 O. E. Trubetskaya, O. A. Trubetskoj, C. Richard, A. M. Vervald, S. A. Burikov, V. V. Marchenkov, O. A. Shenderova, S. V. Patsaeva and T. A. Dolenko, *J. Chromatogr. A*, 2021, **1650**, 462251.
51 X. Zhou, Y. Zhang, C. Wang, X. Wu, Y. Yang, B. Zheng, H. Wu, S. Guo and J. Zhang, *ACS Nano*, 2012, **6**, 6592–6599.
52 M. R. Younis, G. He, J. Lin and P. Huang, *Front. Chem.*, 2020, **8**, 424.
53 R. Tian, S. Zhong, J. Wu, W. Jiang, Y. Shen, W. Jiang and T. Wang, *Opt. Mater.*, 2016, **60**, 204–208.
54 Q. Liu, J. Zhang, H. He, G. Huang, B. Xing, J. Jia and C. Zhang, *Nanomaterials*, 2018, **8**, 844.
55 X. Tong, M. Cherif, G. Zhang, X. Zhan, J. Ma, A. Almesrati, F. Vidal, Y. Song, J. P. Claverie and S. Sun, *ACS Appl. Mater. Interfaces*, 2021, **13**, 30512–30523.
56 M. Havrdova, K. Hola, J. Skopalik, K. Tomankova, M. Petr, K. Cepe, K. Polakova, J. Tucek, A. B. Bourlinos and R. Zboril, *Carbon*, 2016, **99**, 238–248.
57 K.-A. Tsai, P.-Y. Hsieh, T.-H. Lai, C.-W. Tsao, H. Pan, Y.-G. Lin and Y.-J. Hsu, *ACS Appl. Energy Mater.*, 2020, **3**, 5322–5332.
58 C. T. Cao, S.-W. Kim, H. J. Kim, R. Purbia, S. H. Kim, D. Kim, K. J. Choi, H. Park and J. M. Baik, *Nano Energy*, 2022, **96**, 107117.
59 A. Sheini, A. Taherpour, M. Maghsudi, S. Farajmand-Amirabadi, M. Kouchak, N. Rahbar, M. Sabaeian and H. Alidadi, *Colloids Surf., A*, 2022, **636**, 128066.
60 M. Kaur, M. Kaur and V. K. Sharma, *Adv. Colloid Interface Sci.*, 2018, **259**, 44–64.
61 T. Mosmann, *J. Immunol. Methods*, 1983, **65**, 55–63.
62 L. G. Cançado, A. Hartschuh and L. Novotny, *J. Raman Spectrosc.*, 2009, **40**, 1420–1426.

63 C. Rabelo, H. Miranda, T. L. Vasconcelos, L. G. Cancado and A. Jorio, in *2019 4th International Symposium on Instrumentation Systems, Circuits and Transducers (INSCIT)*, IEEE, 2019, pp. 1–6.
64 T. L. Vasconcelos, B. S. Archanjo, B. S. Oliveira, R. Valaski, R. C. Cordeiro, H. G. Medeiros, C. Rabelo, A. Ribeiro, P. Ercius, C. A. Achete, A. Jorio and L. G. Cançado, *Adv. Opt. Mater.*, 2018, **6**, 1800528.
65 B. S. Oliveira, B. S. Archanjo, R. Valaski, C. A. Achete, L. G. Cançado, A. Jorio and T. L. Vasconcelos, *J. Chem. Phys.*, 2020, **153**, 114201.
66 H. Miranda, C. Rabelo, T. L. Vasconcelos, L. G. Cançado and A. Jorio, *Phys. Status Solidi RRL*, 2020, **14**, 2000212.
67 A. Mikhraliieva, V. Zaitsev, O. Tkachenko, M. Nazarkovsky, Y. Xing and E. V. Benvenutti, *RSC Adv.*, 2020, **10**, 31305–31315.
68 C. Hu, T. R. Su, T. J. Lin, C. W. Chang and K. L. Tung, *New J. Chem.*, 2018, **42**, 3999–4007.
69 H. Tilborg, A. Nilsson and N. Mårtensson, *J. Electron Spectrosc. Relat. Phenom.*, 1993, **62**, 73–93.
70 X. Liu, F. Zhao, H. Guo, D. Xia, Z. Dong and Z. Li, *Environ. Sci. Pollut. Res.*, 2022, **29**, 33495–33505.
71 T. L. Vasconcelos, B. S. Archanjo, B. S. Oliveira, W. F. Silva, R. S. Alencar, C. Rabelo, C. A. Achete, A. Jorio and L. G. Cancado, *IEEE J. Sel. Top. Quantum Electron.*, 2021, **27**, 1–11.
72 S. Claramunt, A. Varea, D. López-Díaz, M. M. Velázquez, A. Cornet and A. Cirera, *J. Phys. Chem. C*, 2015, **119**, 10123–10129.
73 A. Maghsoumi, L. Brambilla, C. Castiglioni, K. Müllen and M. Tommasini, *J. Raman Spectrosc.*, 2015, **46**, 757–764.
74 L. Gustavo Cançado, M. Gomes da Silva, E. H. Martins Ferreira, F. Hof, K. Kampioti, K. Huang, A. Pénicaud, C. Alberto Achete, R. B. Capaz and A. Jorio, *2D Mater.*, 2017, **4**, 025039.
75 C. Rabelo, T. L. Vasconcelos, B. C. Publio, H. Miranda, L. G. Cançado and A. Jorio, *Phys. Rev. Appl.*, 2020, **14**, 024056.
76 J. P. Rourke, P. A. Pandey, J. J. Moore, M. Bates, I. A. Kinloch, R. J. Young and N. R. Wilson, *Angew. Chem., Int. Ed.*, 2011, **50**, 3173–3177.
77 Z. Liu, K. Nørgaard, M. H. Overgaard, M. Ceccato, D. M. A. Mackenzie, N. Stenger, S. L. S. Stipp and T. Hassenkam, *Carbon*, 2018, **127**, 141–148.
78 I. S. Raja, A. Molkenova, M. S. Kang, S. H. Lee, J. E. Lee, B. Kim, D.-W. Han and T. S. Atabaev, in *Advances in experimental medicine and biology*, 2022, vol. 1351, pp. 23–39.
79 L. Liang, X. Peng, F. Sun, Z. Kong and J. W. Shen, *Nanoscale Adv.*, 2021, **3**, 904–917.
80 X. Zhao, W. Gao, H. Zhang, X. Qiu and Y. Luo, in *Handbook of Nanomaterials in Analytical Chemistry*, Elsevier, 2020, pp. 493–505.
81 X. Wang, R. Lei, H. Huang, N. Wang, L. Yuan, R. Xiao, L. Bai, X. Li, L. Li and X. Yang, *Nanoscale*, 2015, **7**, 2034–2041.
82 S. Achawi, J. Pourchez, B. Feneon and V. Forest, *Chem. Res. Toxicol.*, 2021, **34**, 2003–2018.
83 S. Wang, I. S. Cole and Q. Li, *RSC Adv.*, 2016, **6**, 89867–89878.
84 Z. M. Markovic, B. Z. Ristic, K. M. Arsikin, D. G. Klisic, L. M. Harhaji-Trajkovic, B. M. Todorovic-Markovic, D. P. Kepic, T. K. Kravic-Stevovic, S. P. Jovanovic, M. M. Milenkovic, D. D. Milivojevic, V. Z. Bumbasirevic, M. D. Dramicanin and V. S. Trajkovic, *Biomaterials*, 2012, **33**, 7084–7092.
85 Z. Tu, K. Achazi, A. Schulz, R. Mülhaupt, S. Thierbach, E. Rühl, M. Adeli and R. Haag, *Adv. Funct. Mater.*, 2017, **27**, 1701837.